Surface plasmon dispersion in a mid-infrared Ge/Si quantum dot photodetector coupled with a perforated gold metasurface

A. I. Yakimov,[1,2,a)] V. V. Kirienko,[1] V. A. Armbrister,[1] A. A. Bloshkin,[1] and A. V. Dvurechenskii[1]
[1]*Rzhanov Institute of Semiconductor Physics, Siberian Branch of the Russian Academy of Science, 630090 Novosibirsk, Russia*
[2]*Tomsk State University, 634050 Tomsk, Russia*

(Received 12 March 2018; accepted 15 April 2018; published online 24 April 2018)

The photodetection improvement previously observed in mid-infrared (IR) quantum dot photodetectors (QDIPs) coupled with periodic metal metasurfaces is usually attributed to the surface light trapping and confinement due to generation of surface plasmon waves (SPWs). In the present work, a Ge/Si QDIP integrated with a metal plasmonic structure is fabricated to experimentally measure the photoresponse enhancement and verify that this enhancement is caused by the excitation of the mid-IR surface plasmons. A 50 nm-thick gold film perforated with a 1.2 μm-period two-dimensional square array of subwavelength holes is employed as a plasmonic coupler to convert the incident electromagnetic IR radiation into SPWs. Measurements of the polarization and angular dependencies of the photoresponse allow us to determine the dispersion of plasmon modes. We find that experimental dispersion relations agree well with that derived from a computer simulation for fundamental plasmon resonance, which indicates that the photodetection improvement in the mid-IR spectral region is actually caused by the excitations of surface plasmon Bloch waves. *Published by AIP Publishing*. https://doi.org/10.1063/1.5029289

It is well known that quantum dot (QD) infrared (IR) photodetectors (QDIPs) have important advantages over quantum well devices. The three-dimensional confinement of the QD structure provides the possibility to suppress the electron-phonon scattering due to the phonon bottleneck effect,[1,2] which leads to a small thermal generation rate and reduced dark current.[3–5] However, despite the aforementioned superior features of QDs, a limitation in conventional QDIPs is that the absorbance of mid-IR radiation is weak, which results from the low density of states coupled to the dots and from the limited QD absorption layer thickness. Several groups have reported photocurrent (PC) enhancement of mid-IR InAs/(In)GaAs[6–14] and Ge/Si(Ge)[15,16] QDIPs using surface plasmon wave (SPW) coupling structures. Metallic films perforated with two-dimensional subwavelength hole arrays (2DHAs) often have been used as the plasmonic couplers. By an analogy with the visible and near-IR regions, where SPWs are widely used to manipulate light on the subwavelength scale, it has been suggested that the excitation of mid-IR SPW modes as well offers an effective surface light trapping, enhancement of local field intensities, and thus interaction with the optically thin device active region. However, a part of the plasmonic community comes around to the argument that traditional metals are not really plasmonic at the mid-IR wavelengths.[17,18] The reason for this can be understood from the following arguments. In efficient plasmonic devices, the real part of the metal permittivity should be negative, and its absolute value must be comparable to that of dielectric components.[19] Unfortunately, metals such as gold and silver have very large negative real permittivity in the mid-IR range[20] and their properties resemble more likely those of near-perfect conductors. At long wavelengths, excited waves are much closer to plane waves than the traditional SPWs, which can be an obstacle in the fabrication of enhanced mid-IR QDIPs. Doped semiconductors,[21] transition-metal nitrides,[17] and transparent conductive oxides[22] with lower losses have been proposed as new plasmonic materials to replace noble metals. Nevertheless, it has been recently demonstrated that the proper figure of merit that characterizes the ability of SPW to achieve a high degree of field confinement with small loss should be the ratio of plasma frequency to the scattering loss, instead of other commonly used material parameters.[23] If this is the case, noble metals even with their high ohmic losses are not likely to be replaced in the foreseeable future and are still good choice for mid-IR plasmonics. In this paper, we study the plasmon dispersion relations in Ge/Si QDIPs integrated with a gold 2DHA plasmonic structure, to verify the existence of mid-IR surface plasmon waves. The measured dispersion curves of the fundamental SPW mode agree well with that derived from a computer simulation and provide evidence of the surface plasmon-like nature of the mid-IR PC enhancement.

The Ge/Si QD samples are grown using a Riber SIVA21 molecular beam epitaxy (MBE) system. A 0.5 μm boron-doped (p+) Si contact layer ($p = 2 \times 10^{18}$ cm^{-3}) is first grown on a Si (100) wafer [Fig. 1(a)]. The active region of QDIPs is composed of ten stacks of Ge quantum dots separated by 40-nm Si barriers and is sandwiched in between the 200-nm-thick undoped buffer and 120-nm-thick cap Si layers. The p-type remote doping of the dots is achieved with a boron δ-doping layer inserted 5 nm above each dot layer. The areal doping density is 6×10^{11} cm^{-2}. Finally, a boron doped 100-nm-thick p^+-Si top contact layer (1×10^{19} cm^{-3}) is grown. After the MBE growth, the wafers are processed into 1.4 mm diameter

a)yakimov@isp.nsc.ru

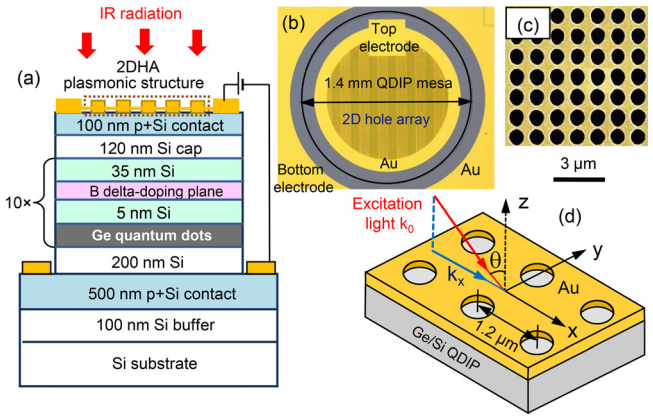

FIG. 1. (a) Layer sequence of the 10-period Ge/Si QDIP enhanced with the top metallic 2DHA plasmonic structure. (b) Optical image of a hybrid Ge/Si photodetector with Ge quantum dots integrated with a 2D square lattice of holes in the gold film on its surface (plan view). A 1D periodicity along the x axis is an artifact of the image. (c) A zoom-in scanning electron microscopy image of the square lattice of circular holes in the Au film. For this sample, the diameter of holes is $d = 0.85 \pm 0.05\,\mu$m and the lattice constant is $a = 1.2\,\mu$m. (d) Schematic view of the top-illuminated 2DHA plasmonic QDIP with an incident angle θ.

circular QDIPs [Fig. 1(b)]. On top of the QDIPs, we fabricate the metallic 2DHA plasmonic structure by the deposition of a 50-nm-thick Au film and formation of a periodic lattice of circular holes using the optical lithography, e-beam metal deposition, and lift-off techniques [Fig. 1(c)]. The 2DHAs have the square lattice symmetry with the measured hole diameter of $d = 0.85 \pm 0.05\,\mu$m. The fast Fourier transform analysis of the 2DHA surface morphology of fabricated samples revealed the well-defined 2DHA periodicity of $a = 1.19 \pm 0.02\,\mu$m in both the x and y directions. A reference QDIP without the surface plasmonic structure is also fabricated for comparison of device performance. Both the plasmonic enhanced and the bare QDIPs are taken from a single die of the same wafer right next to each other. In this work, all measurements are performed at a temperature of 78 K. All devices under test are biased at −1 V. The incident IR light illuminates detectors from their top side. The growth conditions, device processing, and measurement procedures are similar to QDIPs reported before.[15]

Angular photoresponse characterization is used to confirm that the experimentally observed PC enhancement in mid-IR QDIPs coupled with the gold 2DHA is in fact the surface plasmon Bloch wave modes. The dispersion relation of SPWs on a smooth metal-dielectric interface is given by[19]

$$|\mathbf{k}_{sp}| = \frac{\omega}{c}\left(\frac{\varepsilon_m(\omega)\varepsilon_d}{\varepsilon_m(\omega)+\varepsilon_d}\right)^{1/2}, \tag{1}$$

where $\mathbf{k}_{sp}$ is the wavevector of the SPW, ω is the frequency, and $\varepsilon_m(\omega)$ and ε_d are the relative permittivities of the metal and dielectric, respectively. Due to the frequency-dependent dielectric function ε_m, the dispersion curve exhibits nonlinear characteristic.[24] The curve starts at $\omega = 0$ and $k_{sp} = 0$ and gradually approaches an asymptotic limit, the surface plasmon resonant frequency ω_{sp}, when the relative permittivity of the metal and dielectric are of the same magnitude but the opposite sign.

Generation of SP Bloch waves in the corrugated metasurface is allowed when their momentum matches the momentum of the incident photon and the reciprocal lattice vectors characterizing the periodic modulation of the electron density[25,26]

$$\mathbf{k}_{sp} = \mathbf{k}_x \pm i\mathbf{G}_x \pm j\mathbf{G}_y, \tag{2}$$

where $\mathbf{k}_x = |\mathbf{k}_0|\sin\theta$ is the component of the wavevector of the incident radiation in the plane of grating as defined in [Fig. 1(d)], θ is the angle of incidence, $|\mathbf{k}_0| = 2\pi/\lambda$ is the wavevector of the incident radiation, $\mathbf{G}_x$ and $\mathbf{G}_y$ are the reciprocal lattice vectors (for a square lattice, $|\mathbf{G}_x| = |\mathbf{G}_y| = 2\pi/a$), and i and j are the grating orders determining the SPW propagation direction. In this work, dispersion of the plasmon resonance is measured by recording the PC enhancement factor as a function of incident angle θ by tilting the samples in the beam for different light polarizations. The devices are defined to lie in the (x, y) plane. Rotating them around the y axis allows an investigation of the dispersion relations in the $\mathbf{k}_x$ direction. To study the (1, 0) and (0, 1) plasmon modes separately, we measure the photoresponse in the two different light polarizations (see inset of Fig. 3): the radiation was polarized either along the y axis (TE polarization) or in the (x, z) plane (TM polarization).

For a square array of apertures at normal incidence, the resonance SPW wavelengths are given in a first approximation by the grating-coupling equation

$$\lambda_{ij} = \frac{a}{\sqrt{i^2+j^2}}\left(\frac{\varepsilon_m\varepsilon_d}{\varepsilon_m+\varepsilon_d}\right)^{1/2}. \tag{3}$$

For $a = 1.2\,\mu$m, Eq. (3) predicts coupling to the (0, ±1) [or its degenerate mode (±1, 0)] fundamental SPW resonance at $\lambda_0 = 4.1\,\mu$m, and the (1, 1) higher order plasmonic mode is expected at 2.9 μm. Figure 2(a) shows the measured normal-incidence PC spectra of the QDIPs with and without the 2DHA plasmonic structure. Compared with a bare QDIP, the plasmonic detector provides a fourfold photocurrent enhancement at the wavelength of ∼4 μm. The PC enhancement factor is plotted in Fig. 2(b), together with the transmission spectrum taken from the same sample. Both spectra consist of two clearly distinguishable maxima, labeled as A and B, and are peaked near the position of the fundamental SPW mode expected from Eq. (3). The photocurrent maximum is slightly redshifted when compared to the transmission peak due to Fano-type quantum interference between the discrete plasmon resonance and the non-resonant SPW scattering by the holes.[27] The difference of the PC and transmission line shapes has been previously discussed in Ref. 15. At present, the origin of the binary peak structure with a splitting of ∼0.1 μm is unclear and subject to further investigation. The appearance of two closely located maxima cannot be explained by the multiple periodicity of the 2DHA as this disagrees with the result of Fourier analysis of the gold metasurface morphology. We propose that the doublet can be related to a coupling of the SPW modes on both sides of the metal film. Indeed, the SPW penetration depth into the noble metal in the infrared region is about 25 nm,[28] which is comparable with the thickness of the gold layer in our devices (50 nm).

Frequently, the enhanced transmission of metallic 2DHA structures is discussed in terms of a Fano-type

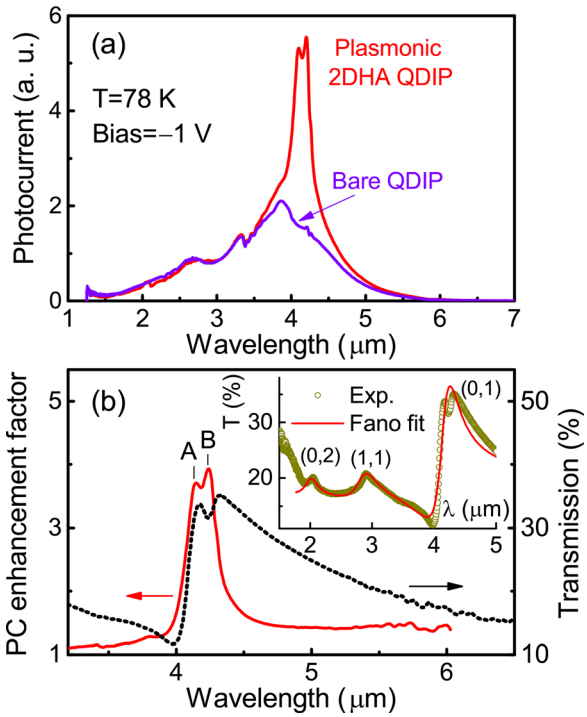

FIG. 2. (a) Photocurrent spectral response of the Ge/Si QDIP with the gold 2DHA plasmonic structure compared to the bare QDIP at normal incident radiation ($\theta = 0°$). The incoming light has no polarization. The PC enhancement at ~4 μm is due to excitation of the resonant fundamental plasmon mode ($i^2 + j^2$). (b) Photocurrent enhancement and transmission spectra. The PC enhancement factor is defined as the ratio of the spectral characteristics of the photocurrent of the plasmonic QDIP and the reference detector. The inset shows the transmission spectrum measured in a wide wavelength range (circles) and the best-fit to the three peak Fano-type lineshape Eq. (4) (red line). The transmission peaks are labeled with the (i, j) grating orders.

interference.[29] Here, we analyze the experimental transmission spectrum using the three peak Fano profile[29]

$$T = \sum_{i=1}^{3} |t_i|^2 \frac{[\epsilon_i + q_i]^2}{1 + \epsilon_i^2}, \tag{4}$$

where $|t_i|^2$ is the non-resonant "Bethe" transmission coefficient, q_i is the dimensionless parameter which describes the ratio between resonant and non-resonant transition amplitudes, ϵ_i is the detuning from the ith resonance given by[29] $\epsilon_i = [\omega - (\omega_i + \Delta_i)]/(\Gamma_i/2)$, ω_i is the resonant frequency, Δ_i is the resonant shift, and Γ_i is the linewidth. The three transmission peaks correspond to the (0, 1) fundamental SPW resonance and the higher-order (1, 1) and (0, 2) modes. The red line in the inset of Fig. 2(b) shows the curve fitting of the transmission spectrum using Eq. (4) with the fitting parameters of $q_1 = -1.8$, $\lambda_1 = 4.2\,\mu$m, $q_2 = -3.2$, $\lambda_2 = 2.9\,\mu$m, and $q_3 = -6.2$, $\lambda_3 = 2.0\,\mu$m. Clearly, the transmission profile agrees well with the three-peak Fano-type interference model.

Figures 3(a) and 3(b) depict typical PC enhancement spectra for different light polarizations and incidence angles. For TE polarization, both peaks A and B slightly shift towards the shorter wavelengths as a function of θ. For TM-polarized radiation, the SPW mode splits into the two peaks which move in the opposite directions with the increasing incidence angle. To identify the spectral peak position more accurately, we decompose each spectrum into two or four

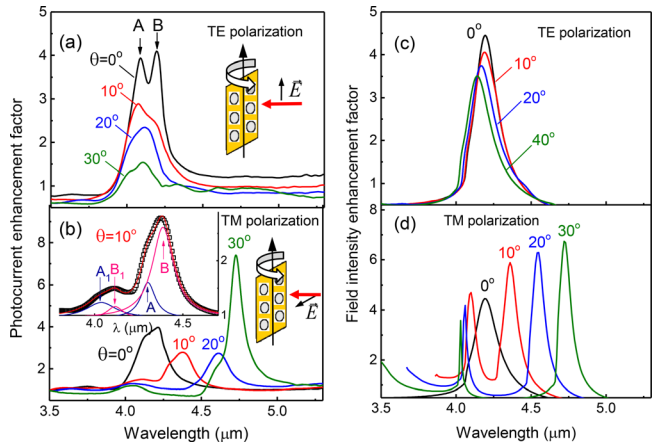

FIG. 3. (a) Photocurrent enhancement spectra as a function of incident angle for light polarized parallel to the axis of rotation (TE polarization). (b) Photocurrent enhancement spectra as a function of incident angle for light polarized orthogonal to the axis of rotation (TM polarization). The inset shows an example of decomposition of the PC enhancement spectrum for $\theta = 10°$ into four Lorentzian functions, labeled as A, B, A_1, and B_1. (c) and (d) Calculated near-field intensity enhancement over the QD active region for (c) TE and (d) TM polarization at different excitation angles.

Lorentzian profiles. The inset of Fig. 3(b) demonstrates an example of such a procedure for $\theta = 10°$. To get insight into the angular-resolved SPW modes, we perform a numerical simulation of the plasmonic structure under study. The SPW and the near-field component distributions are calculated with the 3D finite-element frequency-domain (FEFD) method[30,31] based commercial software Comsol Multiphysics by numerically solving the Maxwell equations.[32] We use the periodical boundary conditions that allow the plasmonic structure to cover an infinite large area. The simulated structure is a square hole array in a layer of Au on a Si crystal. The diameter of the hole is 0.8 μm, the 2DHA period is 1.2 μm, and the thickness of the Au layer is 50 nm. The plane wave radiation with a linear polarization falls on the top of the QDIP at various angles of incidence θ. The air and Si regions are modeled using rectangular parallelepiped geometry with correspondent refractive indices. The grid-independence of the results has been verified by doubling the number of elements in the simulation. The near-field intensity enhancement factor is quantified by dividing the field intensity integrated over the QD active region $\int_V |E|^2 dV$ by that in the sample without a holey gold film.[12,15] The calculated enhancement spectra are shown in Figs. 3(c) and 3(d). The theoretical data agree well with the experimental spectra in both the angular dependence of resonance wavelength and amplitude.

The dispersion of the PC enhancement maximum is shown in Fig. 4, together with the energies of the fundamental plasmon mode obtained from a numerical simulation (solid lines). The average position of peaks A and B (or A_1 and B_1) is considered as the position of the photocurrent peak. Theoretical values of plasmon resonance energies are determined from the peak wavelengths of the near-field intensity enhancement factor. The dispersive behavior is clearly seen in Fig. 4. The agreement between the angular-dependent positions of PC enhancement maximum and numerical simulation is perfect for all branches (–1, 0), (+1, 0), and (±0, 1). To analyze the dispersion characteristics, we rewrite the

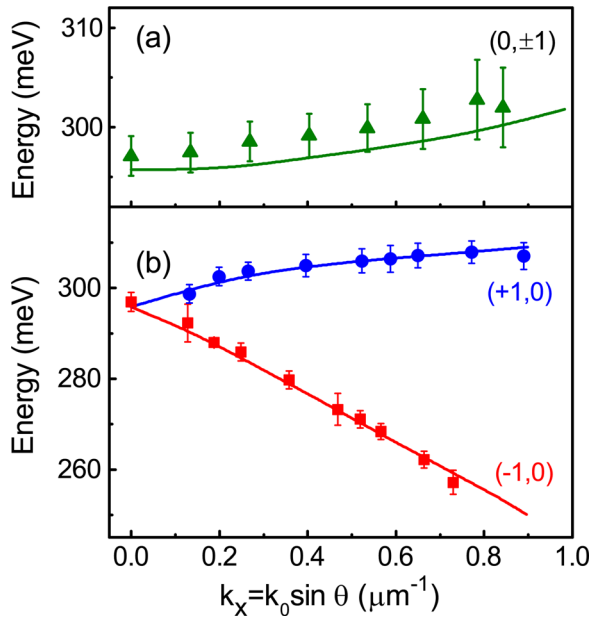

FIG. 4. Dispersion of the plasmon modes with $i^2+j^2=1$ (symbols) for different branches (i, j) obtained by recording the peak energies as a function of k_x for (a) TE and (b) TM incident beam polarization. As the position of the PC enhancement maximum, we plot the average position of peaks A and B (or A_1 and B_1). The peak notation A, B, A_1, and B_1 is explained in the inset of Fig. 3(b). The error bars in the energy axis represent the uncertainty of the fitting the experimental spectra to Lorentzian functions. Additionally shown are the dispersion curves of the fundamental plasmon resonance computed in an FEFD simulation (solid lines).

vector expression (2) in a form appropriate for the absolute values of wavevectors

$$k_{sp}=\sqrt{\left(k_x\pm i\frac{2\pi}{a}\right)^2+\left(j\frac{2\pi}{a}\right)^2}. \tag{5}$$

Equation (5) yields $k_{sp}=2\pi/a-k_x$, $k_{sp}=k_x+2\pi/a$, and $k_{sp}=\sqrt{k_x^2+(2\pi/a)^2}$ for the (–1, 0), (+1, 0), and (0, ±1) branches, respectively. These predictions are in good agreement with the data presented in Fig. 4. As the angle of incidence increases, the degeneracy of the (–1, 0) and (+1, 0) SPW modes is lifted. The (–1, 0) mode moves towards smaller photon energy with increasing k_x, while the (+1, 0) and (0, ±1) modes are blueshifted. Since the SPW frequency is a sublinear function of wavevector and tends to saturate at large ω [see, Eq. (1)], the (+1, 0) resonance demonstrates a weaker dispersion than the (–1, 0) mode. The measured dispersion relations are very similar to those obtained from the measurements of extraordinary transmission gratings in the visible,[33] near,[34,35] and mid-IR[36] regions, which indicates that the photocurrent enhancement in mid-IR QDIPs is caused by excitations of surface plasmon Bloch waves.

Notice that excitation of the long-wave (–1, 0) resonance at large θ yields the PC enhancement higher than that produced by the short-wave (+1, 0) and (0, ±1) SPW modes (Fig. 3). We suppose that this phenomenon can be explained by the wavelength dependence of the SPW penetration depth inside the absorption layer. The field penetration depth δ_d into the dielectric becomes larger as the photon wavelength λ is increased[28]

$$\delta_d=\frac{\lambda}{2\pi}\sqrt{\frac{\varepsilon_m'+\varepsilon_d}{\varepsilon_d^2}}, \tag{6}$$

where ε_m' is the real permittivity of the metal. As a result, a better spatial matching of the vertical extent of the plasmonic field to the QD region can be achieved and larger near-field intensity and photocurrent enhancement can be observed,[8,10] in agreement with Fig. 3.

In summary, a mid-infrared Ge/Si quantum dot photodetector with the top 2DHA gold plasmonic structure was fabricated. A four times improvement in photocurrent is observed at wavelengths of the fundamental plasmonic mode. Measurements of the mode's dispersion curves allow us to conclude that the surface plasmon waves due to the interaction of the light with the grating remain the dominant element of the detector photoresponse enhancement in the mid-IR spectral region.

This study was supported by the Russian Foundation for Basic Research (Project No. 16-29-03024). The part of the work associated with fabrication of plasmonic structures was also supported by Presidium of the Russian Academy of Science via Grant No. 0306-2018-0008.

[1]U. Bockelmann and G. Bastard, Phys. Rev. B **42**, 8947 (1990).
[2]H. Benisty, C. M. Sotomayor-Torrés, and C. Weisbuch, Phys. Rev. B **44**, 10945 (1991).
[3]P. Bhattacharya, X. H. Su, S. Chakrabarti, G. Ariyawansa, and A. G. U. Perera, Appl. Phys. Lett. **86**, 191106 (2005).
[4]X. Lu, J. Vaillancourt, and M. J. Meisner, Semicond. Sci. Technol. **22**, 993 (2007).
[5]F.-J. Wang, N. Zhuo, S.-M. Liu, F. Ren, Z.-D. Ning, X.-L. Ye, J.-Q. Liu, S.-Q. Zhai, F.-Q. Liu, and Z.-G. Wang, Appl. Phys. Lett. **108**, 251103 (2016).
[6]S. C. Lee, S. Krishna, and S. R. J. Brueck, Opt. Express **17**, 23160 (2009).
[7]S. C. Lee, S. Krishna, and S. R. J. Brueck, Appl. Phys. Lett. **97**, 021112 (2010).
[8]C.-C. Chang, Y. D. Sharma, Y.-S. Kim, J. A. Bur, R. V. Shenoi, S. Krishna, D. Huang, and S.-Y. Lin, Nano Lett. **10**, 1704 (2010).
[9]P. Vasinajindakaw, J. Vaillancourt, G. Gu, and X. Lu, Semicond. Sci. Technol. **27**, 065005 (2012).
[10]R. Liu, P. Vasinajindakaw, G. Gu, J. Vaillancourt, and X. Lu, J. Appl. Phys. D: Appl. Phys. **46**, 015102 (2013).
[11]G. Gu, J. Vaillancourt, P. Vasinajindakaw, and X. Lu, Semicond. Sci. Technol. **28**, 105005 (2013).
[12]G. Gu, J. Vaillancourt, and X. Lu, Opt. Express **22**, 24970 (2014).
[13]J. Vaillancourt, N. Mojaverian, and X. Lu, IEEE Photonics Technol. Lett. **26**, 745 (2014).
[14]Y. Zhang, J. Vaillancourt, G. Gu, W. Guo, and X. Lu, J. Appl. Phys. **119**, 193103 (2016).
[15]A. I. Yakimov, V. V. Kirienko, A. A. Bloshkin, V. A. Armbrister, and A. V. Dvurechenskii, J. Appl. Phys. **122**, 133101 (2017).
[16]A. I. Yakimov, V. V. Kirienko, A. A. Bloshkin, V. A. Armbrister, A. V. Dvurechenskii, and J.-M. Hartmann, Opt. Express **25**, 25602 (2017).
[17]G. V. Naik, J. Kim, and A. Boltasseva, Opt. Mater. Express **1**, 1090 (2011).
[18]S. Law, V. Podolskiy, and D. Wasserman, Nanophotonics **2**, 103 (2013).
[19]S. Hayashi and T. Okamoto, J. Phys. D: Appl. Phys. **45**, 433001 (2012).
[20]A. D. Rakić, A. B. Djurišić, J. M. Elazar, and M. L. Majewski, Appl. Opt. **37**, 5271 (1998).
[21]M. Shahzad, G. Medhi, R. E. Peale, W. R. Buchwald, J. W. Cleary, R. Soref, G. D. Boreman, and O. Edwards, J. Appl. Phys. **110**, 123105 (2011).
[22]M. A. Noginov, L. Gu, J. Livenere, G. Zhu, A. K. Pradhan, R. Mundle, M. Bahoura, Y. A. Barnakov, and V. A. Podolskiy, Appl. Phys. Lett. **99**, 021101 (2011).
[23]J. B. Khurgin, Philos. Trans. R. Soc. A **375**, 20160068 (2017).

[24]J. Zhang, L. Zhang, and W. Xu, J. Phys. D: Appl. Phys. **45**, 113001 (2012).
[25]T. W. Ebbesen, H. J. Lezec, H. F. Ghaemi, T. Thio, and P. A. Wolf, Nature **391**, 667 (1998).
[26]C. Genet and T. W. Ebbesen, Nature **445**, 39 (2007).
[27]P. Vasinajindakaw, J. Vaillancourt, G. Gu, R. Liu, Y. Ling, and X. Lu, Appl. Phys. Lett. **98**, 211111 (2011).
[28]W. L. Barnes, J. Opt. A: Pure Appl. Opt. **8**, S87 (2006).
[29]C. Genet, M. P. van Exter, and J. P. Woerdman, Opt. Commun. **225**, 331 (2003).
[30]J. Smajic, C. Hafner, L. Raguin, K. Tavzarashvili, and M. Mishrikey, J. Comput. Theor. Nanosci. **6**, 763 (2009).
[31]N. C. Lindquist, P. Nagpal, K. M. McPeak, D. J. Norris, and S.-H. Oh, Rep. Prog. Phys. **75**, 036501 (2012).
[32]COMSOL Group, http://www.comsol.com for COMSOL Multiphysics Modeling 4.3.
[33]J. Braun, B. Compf, T. Weis, H. Giessen, and M. Dressel, Phys. Rev. B **84**, 155419 (2011).
[34]H. F. Ghaemi, T. Thio, D. E. Grupp, T. W. Ebbesen, and H. J. Lezec, Phys. Rev. B **58**, 6779 (1998).
[35]H. Gao, W. Zhou, and T. W. Odom, Adv. Funct. Mater. **20**, 529 (2010).
[36]T. Ribaudo, D. C. Adams, B. Passmore, E. A. Shaner, and D. Wasserman, Appl. Phys. Lett. **94**, 201109 (2009).